Origin and significance of Si and O isotope heterogeneities in Phanerozoic, Archean, and Hadean zircon

Dustin Trail[a,b,1], Patrick Boehnke[c,d], Paul S. Savage[e], Ming-Chang Liu[b], Martha L. Miller[a], and Ilya Bindeman[f]

[a]Department of Earth & Environmental Sciences, University of Rochester, Rochester, NY 14627; [b]Department of Earth, Planetary, and Space Sciences, University of California, Los Angeles, CA 90095; [c]Department of the Geophysical Sciences, The University of Chicago, Chicago, IL 60637; [d]Chicago Center for Cosmochemistry, Chicago, IL 60637; [e]School of Earth and Environmental Sciences, University of St Andrews, St Andrews KY16 9AJ, United Kingdom; and [f]Department of Earth Sciences, University of Oregon, Eugene, OR 97403

Hydrosphere interactions and alteration of the terrestrial crust likely played a critical role in shaping Earth's surface, and in promoting prebiotic reactions leading to life, before 4.03 Ga (the Hadean Eon). The identity of aqueously altered material strongly depends on lithospheric cycling of abundant and water-soluble elements such as Si and O. However, direct constraints that define the character of Hadean sedimentary material are absent because samples from this earliest eon are limited to detrital zircons ($ZrSiO_4$). Here we show that concurrent measurements of Si and O isotope ratios in Phanerozoic and detrital pre-3.0 Ga zircon constrain the composition of aqueously altered precursors incorporated into their source melts. Phanerozoic zircon from (S)edimentary-type rocks contain heterogeneous $\delta^{18}O$ and $\delta^{30}Si$ values consistent with assimilation of metapelitic material, distinct from the isotopic character of zircon from (I)gneous- and (A)norogenic-type rocks. The $\delta^{18}O$ values of detrital Archean zircons are heterogeneous, although yield Si isotope compositions like mantle-derived zircon. Hadean crystals yield elevated $\delta^{18}O$ values (vs. mantle zircon) and $\delta^{30}Si$ values span almost the entire range observed for Phanerozoic samples. Coupled Si and O isotope data represent a constraint on Hadean weathering and sedimentary input into felsic melts including remelting of amphibolites possibly of basaltic origin, and fractional addition of chemical sediments, such as cherts and/or banded iron formations (BIFs) into source melts. That such sedimentary deposits were extensive enough to change the chemical signature of intracrustal melts suggests they may have been a suitable niche for (pre)biotic chemistry as early as 4.1 Ga.

Hadean | zircon | weathering | silica cycle | origin of life

In the apparent absence of a pre–4.0-Ga terrestrial rock record, early speculations about the Hadean Earth (∼4.5–4.0 Ga) were drawn from meteorites and backward extrapolation of preserved Archean rocks. Insights into the nature of the Hadean surface environment relied on broad estimates of mantle heat production and its transport to the surface, and scaling of the lunar impact record to the early Earth (1). Laboratory simulations predicted intense meteorite bombardment and a thick steam-rich atmosphere (2), suggesting that Earth may not have been continuously habitable in the first 500 My (3).

The first direct constraints on the geology of the young Earth came from the discovery of Hadean detrital zircons (4). Subsequent in situ oxygen isotope measurements of some Hadean zircon yielded isotopically heavy compositions, relative to the canonical mantle value (5, 6). Such isotopic shifts provide evidence for water–rock interactions at low temperatures (*sensu lato*), followed by remelting and incorporation of these signatures into Hadean zircon parent melts by 4.2–4.3 Ga (5–8). More recent numerical calculations that evaluate early Earth heat transfer and plausible chemical reactions (9), the thermal effects of terrestrial impact metamorphism (10), and a reevaluation of lunar impact chronology (11) continue to strengthen the case of a continuously habitable planet shortly after accretion.

Such discoveries are important, although many uncertainties remain regarding Earth's earliest development. This highlights the need to find new ways to better constrain Earth's primordial geology. For instance, only limited information about the identity of weathered material involved in zircon source melts is provided by mildly elevated Hadean zircon $\delta^{18}O$ values, which are up to ∼2‰ above present-day mantle zircon. This is because almost all surficial/low-temperature water–rock interactions result in an isotopically heavy O composition being imparted on the rock. Constraining the identity of weathered Hadean material is timely due to the suggestion that an isotopically light carbon inclusion in an ∼4.1-Ga zircon may indicate the presence of a biosphere (12), implying the need for a suitable substrate for life by this time.

Silicon isotopes, like O isotopes, are also strongly fractionated during chemical weathering of silicate material or low-temperature water–rock interactions (*SI Appendix*, Fig. S1). Given the dominance of O and Si in the lithosphere, the composition of altered or weathered products strongly depends on reactions that involve both elements. First, consider that neoformation of clay minerals prefers the lighter Si isotopes, and the degree of fractionation is magnified with the extent of weathering degree/amount of desilicification to more negative $\delta^{30}Si$ values (i.e., 1:1 clays such as kaolinite are much lighter than 2:1 clay minerals, 13–15). This gives Si isotopes the added advantage over O isotopes alone as they have the potential to be a definitive proxy for identifying the

presence of pelitic sediment in a melt source (Fig. 1, path 1). Second, unlike O isotopes, Si isotopes are unaffected during hydration of primary silicates (i.e., serpentinization) and at low weathering degrees, where igneous minerals still dominate the Si isotope signature (ref. 16 and Fig. 1, path 2). Third, precipitation and diagenesis of authigenic silica and hydrothermal silicification can lead to large variations in $\delta^{30}Si$ (17–19). Under non-equilibrium conditions, this can generate negative shifts in $\delta^{30}Si$, but unlike desilicification, often there may be no correlation between Si and O variations in the silica, due to the different behavior of these elements under different rock/water ratios and temperatures (18). Finally, Si isotopes have another advantage over O isotopes alone because seawater-derived authigenic silica (i.e., chert) reveals uniquely heavy Si isotope compositions (e.g., ref. 20 and Fig. 1, path 3). These Si–O isotope fractionation pathways—shown schematically in Fig. 1—demonstrate the critical advantage of coupled Si–O isotope analysis.

Melt assimilation of the weathered products described above may be used to explore past environments only if the isotopic composition of the whole rock (WR) and minerals—including zircon—partially, at least, reflect these original altered products. Such variations in WR Si isotope compositions, linked unequivocally to source variation, have been measured in several localities, including the Lachlan Fold Belt (21, 22). Moreover, there is limited Si isotope fractionation caused by partial melting and igneous fractional crystallization; mantle rocks and mantle-derived melts yield identical $\delta^{30}Si$ values [bulk silicate Earth (BSE) $\delta^{30}Si = -0.29 \pm 0.07‰$ relative to NBS28; 15]. Felsic rocks, absent of any nonigneous assimilant, tend to be only 0.10–0.20‰ heavier than BSE, demonstrating there is a small and crucially predictable enrichment of heavier Si isotopes due to magmatic differentiation (23). A source rock signature will be recorded in zircons, provided that the difference between $\delta^{30}Si(WR)$ and $\delta^{30}Si(zircon)$—i.e., $\Delta^{30}Si(WR-zircon)$—is constrained.

To extend the terrestrial Si isotope record back to the Hadean, we take the approach that $\delta^{30}Si$ values should be considered with $\delta^{18}O$, because such coupled isotopic analyses are potentially powerful in identifying the lithologies assimilated in Hadean melt sources (Fig. 1). In this paper, we report solution-based multicollector inductively coupled plasma mass spectrometry (MC-ICP-MS) measurements of mantle-derived zircon and separate felsic WR fractions from the crust to define: (i) the Si isotopic composition of zircon that crystallized in the absence of

sediment inputs; and (ii) $\Delta^{30}Si(WR-zircon)$, which constrains high-temperature Si isotope fractionations. To analyze single zircons at ~20-μm spatial resolution, we developed an ion microprobe analytical protocol for simultaneous in situ measurements of both isotope systems. First, this method was used to investigate coupled Si and O isotope compositions of in-context igneous zircons from 10 different Australian Lachlan Fold Belt (LFB) Phanerozoic granitoids classified as (S)edimentary, (I)gneous, and (A)norogenic (*SI Appendix*, Fig. S2). These data, together with the Si and O isotope record of Eoarchean sediments (17, 20), form the basis for our interpretation of ion microprobe data for Hadean and Archean zircon. An overview of measured samples is presented in *SI Appendix*, Table S1.

Results

Mantle-derived Mud Tank carbonatite (Australia), Kimberley Pool (South Africa), and Orapa Kimberlite (Botswana) zircons yield $\delta^{30}Si_{NBS28}$ values that range from −0.34 to −0.41‰ (*SI Appendix*, Table S2). The average $\delta^{30}Si$ value of −0.38 ± 0.02‰ (1 SD), determined by MC-ICP-MS, is used to define $\delta^{30}Si$ of mantle-derived zircon. The LFB Jindabyne tonalite fractions yield respective $\delta^{30}Si$ values for zircon, WR, and quartz of −0.57 ± 0.02, −0.20 ± 0.03, and −0.11 ± 0.02‰. This defines $\Delta^{30}Si(WR-zircon) = 0.37‰$ for this sample (Fig. 2), in good agreement with ab initio Si isotope fractionation calculations (24).

Ion microprobe zircon Si isotope data reveal differences, albeit with overlap, between our Australian LFB granitoid types (Fig. 3 and *SI Appendix*, Table S3). Typically, S-type samples contain $\delta^{30}Si$ values that extend to more negative values than I- or A-type granitoids. In the most extreme cases, zircon $\delta^{30}Si$ extends down to about −1.5‰, as observed for the Cootralantra samples. Zircons analyzed from the Bullenbalong S-type granitoid are not characterized by $\delta^{30}Si$ values lighter than −1.0‰, and in fact the overall distribution of $\delta^{30}Si$ makes it broadly comparable to the $\delta^{30}Si$ range of other I-type zircons. The Cowra Granodiorite contains zircon $\delta^{30}Si$ that would be most consistent with results obtained from I-type samples, except that a larger fraction of the analyses is shifted toward more negative values than other I types examined thus far. I-type granitoids have a similar dispersion in $\delta^{30}Si$ as S types, although zircon $\delta^{30}Si$ distributions are shifted toward heavier values, and several data are within error of 0‰. Except for Cowra zircons, no S-type analyses are within error of 0‰. The A-type sample (Watergums) and Duluth Gabbro yield tighter $\delta^{30}Si$ distributions compared with I- and S-type ranges for a similar number of data points. S- and I-type O isotope data, collected "simultaneously" with Si isotopes, also show distinct differences (Fig. 4 and *SI Appendix*, Fig. S4). S-type zircons typically yield $\delta^{18}O_{VSMOW}$ (Vienna Standard Mean Ocean Water) values from +8–10.5‰, whereas I- and A types are typically confined to $\delta^{18}O$ values of +6–8.5‰.

Individual ion microprobe spot data ($n = 79$) for Jack Hills zircons consist of 14 zircons ≥4.0 Ga and 21 Archean grains (*SI Appendix*, Table S4), and reveal subtle isotopic differences among the two age groups (Fig. 5 and *SI Appendix*, Fig. S4). Specifically, the Archean zircon $\delta^{18}O$ values are between +5.2 and +6.8‰, comparable to previous Jack Hills zircon studies (25). The $\delta^{30}Si$ values of Archean zircon are broadly confined to those like mantle-derived zircon. Most Hadean samples yield $\delta^{18}O$ values that range from +6–7‰ and same grains exhibit both enrichments and depletions in ^{30}Si relative to mantle zircon and show a broadly similar range as Phanerozoic zircon.

Discussion

Phanerozoic "In-Context" Zircons. The well-studied LFB represents an ideal test target to demonstrate in situ zircon-scale investigations. Coupled Si and O isotope studies of zircon have not been conducted previously, so an obvious question is whether these zircon data lead to broadly similar interpretations
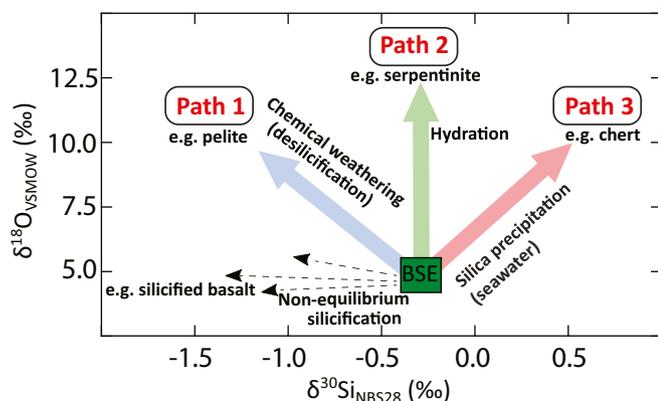
Fig. 1. Schematic cartoon of Si and O isotope covariation during fluid alteration and precipitation processes. Chemical weathering, hydration, seawater silica precipitation, may have different trajectories in Si–O isotope space. Note that "nonequilibrium silicification" has no specific vector or slope as this process can be highly variable due to the different behavior of these elements under different rock/water ratios and at different temperatures (19). BIFs may be enriched in ^{18}O and depleted in ^{30}Si (not shown).

Trail et al.
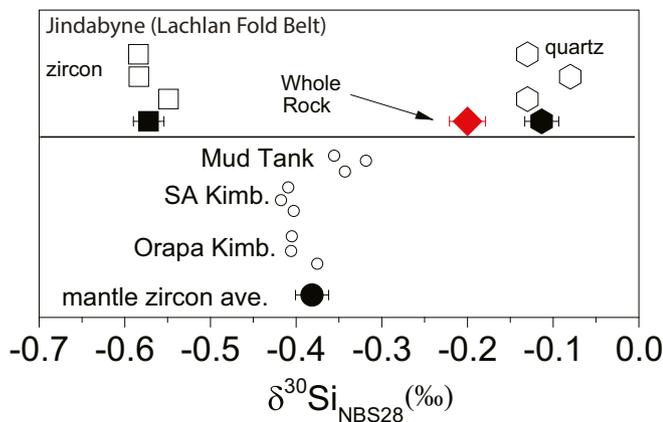
Fig. 2. Our MC-ICP-MS results showing that mantle-derived zircon megacrysts Mud Tank carbonatite (Australia), Kimberley pool (South Africa), and Orapa Kimberlite (Botswana) yield an average $\delta^{30}Si$ value of $-0.38 \pm 0.02‰$ (1 SD). (*Top*) The Si isotopic difference between zircon, quartz, and WR for the LFB I-type Jindabyne tonalite analyzed here is shown; $\Delta^{30}Si$(WR-zircon) is 0.37‰.

compared with WR geochemical studies. The WR Si isotope data show that S-type granitoids are, on average, isotopically lighter than I- and A-type samples, although the range of Si isotopes in S-type granitoid WR extends to lower and slightly higher $\delta^{30}Si$ values than the other two granitoid types (ref. 21 and *SI Appendix*, Fig. S1).

Using felsic rock isotope fractionation relationships of $\Delta^{18}O$ (WR-zircon) $\sim 2‰$ (26), and $\Delta^{30}Si$(WR-zircon) $\sim 0.37‰$ (Fig. 2), we find that S-type zircon, on average, predicts the most negative WR $\delta^{30}Si$ and most elevated $\delta^{18}O$ WR values. This result is consistent with assimilation of pelitic material (e.g., Fig. 1, path 1), and WR data for the region (20). For example, averaging the results from S-type Shannons Flat zircons (Fig. 3 and *SI Appendix*, Fig. S3) predicts respective WR $\delta^{30}Si$ and $\delta^{18}O$ values of $-0.45‰$ and $+10.4‰$. A $\delta^{30}Si$ value of $-0.45‰$ is the lowest estimated WR value of the 10 granitoids explored here, and is in broad agreement with the lowest WR $\delta^{30}Si$ values so far reported in the LFB (*SI Appendix*, Fig. S1). Moreover, predicted WR values from S-type zircons imply another sedimentary source besides Ordovician sediments in close association with the LFB granitoids, also consistent with conclusions reached using WR data only (21). Similar agreement is found for oxygen isotopes (27); other WR isotope calculations for the different granitoids are reported in *SI Appendix*, Table S3. What is also evident, especially for the I-type zircons, is the presence of an isotopically heavy Si source in some regions of the LFB (e.g., Fig. 3; Glenbog). We speculate that this is due to fractional crystallization and seawater-derived authigenic silica (Fig. 1; path 3). In the latter case, silica assimilation will not drive any resulting melt into the peraluminous field nor would it be likely to affect Sr and Nd isotope compositions; hence, the rock will still resemble an I type, even with the anatexis of "nonigneous" material.

If individual data points are considered in lieu of averages, I- and S-type zircon Si- and O isotopes imply heterogeneous isotopic values for the source rocks (Fig. 4). This is particularly marked compared with histogram ranges defined by Duluth Gabbro and A-type Watergums zircon Si and O isotope data (Fig. 3 and *SI Appendix*, Fig. S3). The petrogenesis of zircon in gabbros and A-type melts is typically linked to a single (generally primitive) melt composition which evolved via fractional crystallization. This homogeneous, "primitive" melt composition is well reflected in both suites by their mantle-like Si isotope compositions ($\delta^{30}Si \sim -0.35‰$) and normal distribution (Fig. 3). In contrast, the S- and I-type LFB zircons both define wider, often nonnormal, data distributions. Although the lower analytical

precision of in situ measurements contributes to the apparent range, if all zircons from each I- and S-type melt had an identical Si isotope composition (with perhaps minor variations due to
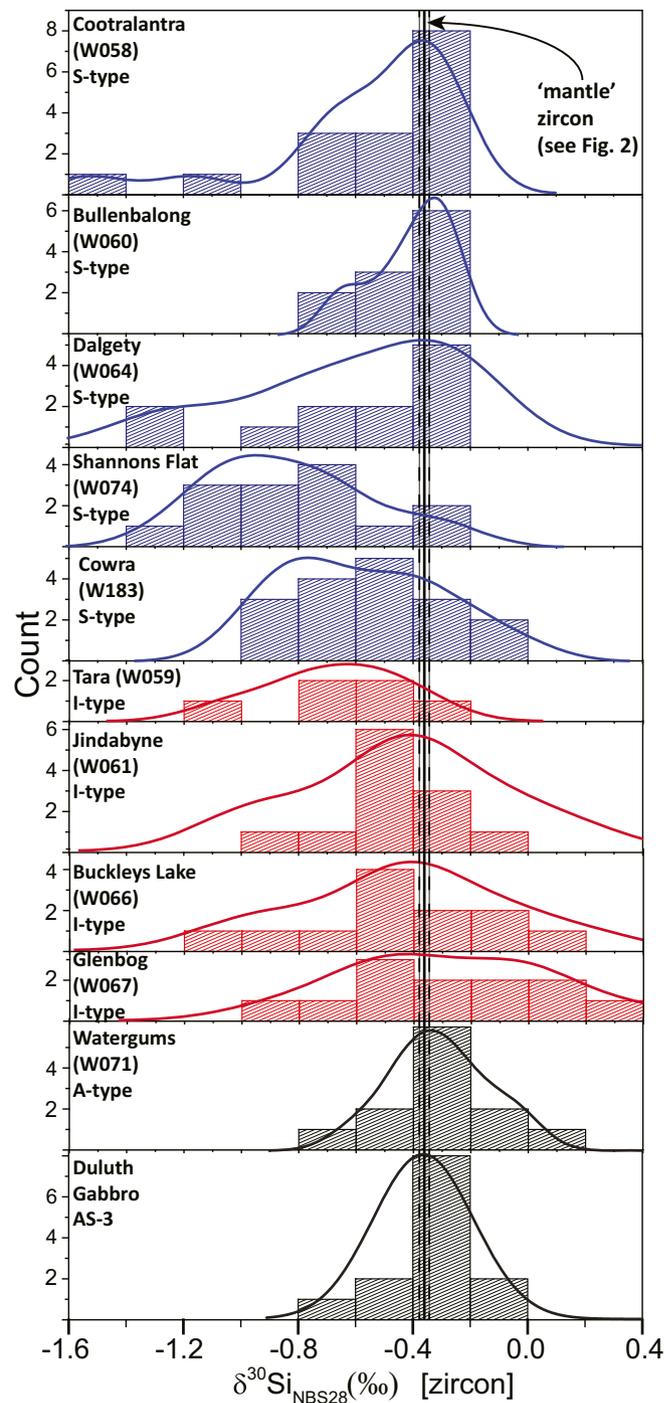
Fig. 3. Histograms showing $\delta^{30}Si$ differences of zircons from 10 LFB granitoids and the Duluth Gabbro (*SI Appendix*, Table S3). The bin sizes are 0.2‰, commensurate with the 1 SE of our ion microprobe measurements. Some S types contain measured $\delta^{30}Si$ values down to $-1.5‰$, while W060, for example, is largely indistinguishable from the $\delta^{30}Si$ of our I-type samples. The A type and zircons show broadly restricted ranges in $\delta^{30}Si$, compared with S- and I-type zircons. WR $\delta^{30}Si$ for S-, I-, and A-type LFB granitoids (21) can be found in *SI Appendix*, Fig. S1. The mantle zircon field is $-0.38 \pm 0.02‰$, after Fig. 2. Histograms for zircon $\delta^{18}O$ values from individual hand samples can be found in *SI Appendix*, Fig. S3.
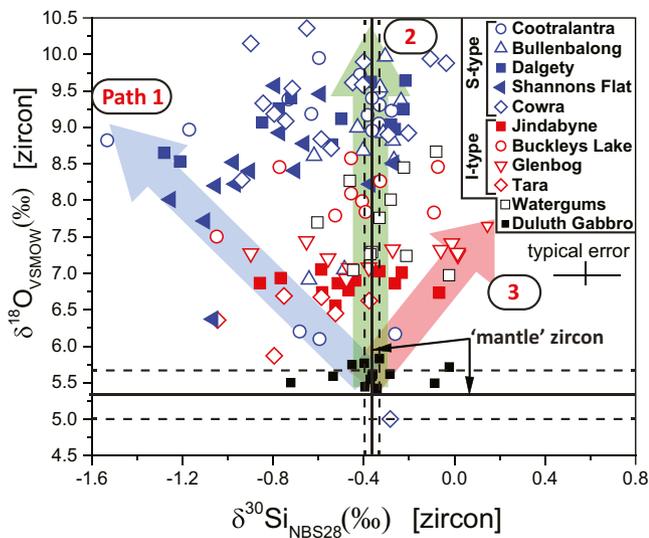
Fig. 4. Zircon LFB $\delta^{18}O$ vs. $\delta^{30}Si$, with annotated path trajectories after Fig. 1. The mantle zircon fields are +5.3 ± 0.3‰ and −0.38 ± 0.02‰ for $\delta^{18}O$ (59) and $\delta^{30}Si$ (Fig. 2), respectively. Average $\delta^{18}O$ values for S-type zircons are +8.8‰, consistent with a WR value of $\delta^{18}O$ >10‰ (27). The zircon $\delta^{18}O$ values from I-type rocks yield average values +7.5‰, consistent with WR values of <10‰ (*SI Appendix*, Table S3). Path 2 may also indicate a balance between assimilation/derivation between chert-like, "path 3" and pelite-like "path 1" protoliths, both of which have high $\delta^{18}O$.

fractional crystallization), data distributions similar to that of the A-type or gabbroic zircons are expected. Hence, the wider I- and S-type zircon Si and O isotope range likely reflects heterogeneities in the source, or possibly multiple melt sources. This incomplete homogenization of multiple source materials in the Lachlan samples is also observed in Nd-, Sr-, and O-isotope WR and mineral studies, which underscores the hybrid nature of felsic natural systems (27, 28).

Hadean and Archean (Detrital) Zircons. Several zircons yield $\delta^{30}Si$ values indistinguishable from mantle-derived zircon, but with heavier $\delta^{18}O$ than the mantle (Fig. 5). These zircons may have crystallized from melts that included assimilation of hydrated/serpentinized basalt, whereby the original "igneous" Si isotope composition of the host rocks remained unaltered, (e.g., Fig. 1, path 2). Alternatively, it was suggested that low fluid/rock ratios could generate positive O isotope excursions without accompanying Si isotope variation (19). Both scenarios are consistent with Hadean melts (partially) influenced by source material altered by considerable hydrothermal activity.

Perhaps the most intriguing Hadean zircon yields a mantle-like $\delta^{18}O$ value of +5.49‰, but records a $\delta^{30}Si$ value of −1.13‰ (grain 1–10). This grain represents our strongest evidence for a Hadean Si reservoir out of equilibrium with the mantle. Evaluation of the $\delta^{18}O$ value only would lead to the conclusion that this grain shows no evidence for interaction with an aqueous reservoir, whereas $\delta^{30}Si$ suggests otherwise. We rule out fractional crystallization, as $\Delta^{30}Si$(WR-zircon) is ~0.35‰ for felsic systems; this relationship implies a WR value of ~-0.75‰. To explain this result, we turn to the Archean Si isotope sedimentary record.

Archean cherts, which formed by chemical precipitation (and reprecipitation), have Si isotope values as low as ~−3‰, which also applies to Archean banded iron formations (BIFs) (17, 29–31). These sediments are typically assumed to result in ^{18}O-enriched material compared with the mantle (20), meaning that an ^{18}O-depleted reservoir is also required to balance the mantle-like zircon value of +5.49‰. The Fe-oxide phases in BIFs are one possibility; these may be ^{18}O-depleted (32), which

is also supported by low-temperature Fe-oxide-H_2O oxygen isotope equilibrium fractionations (33). Also, alteration of mafic rocks by seawater can either enrich or deplete the resulting product in ^{18}O; higher-temperature (postsolidus) exchange with seawater decreases the $\delta^{18}O$ value of the altered rock (34, 35). This reasoning assumes that seawater $\delta^{18}O$ was ~0‰, similar to modern (35), which is based on an assumed balance of hydrothermal and weathering fluxes (36). Alternatively, at far-from-equilibrium conditions (e.g., dashed arrows in Fig. 1), light Si isotope compositions have been recorded in chemical precipitates where no large variations in O have been recorded (37). We propose that burial and anatexis of a succession of oceanic lithologies (cherts, BIFs, and/or altered mafic rocks) as a possible explanation for the chemistry of this 4.05-Ga zircon. A simple end-member Si isotope mixing model with basalt and chemical sediment (e.g., chert) requires less than 20% of the latter to explain the range of $\delta^{30}Si$ values observed in detrital zircons (*SI Appendix*, Fig. S5).
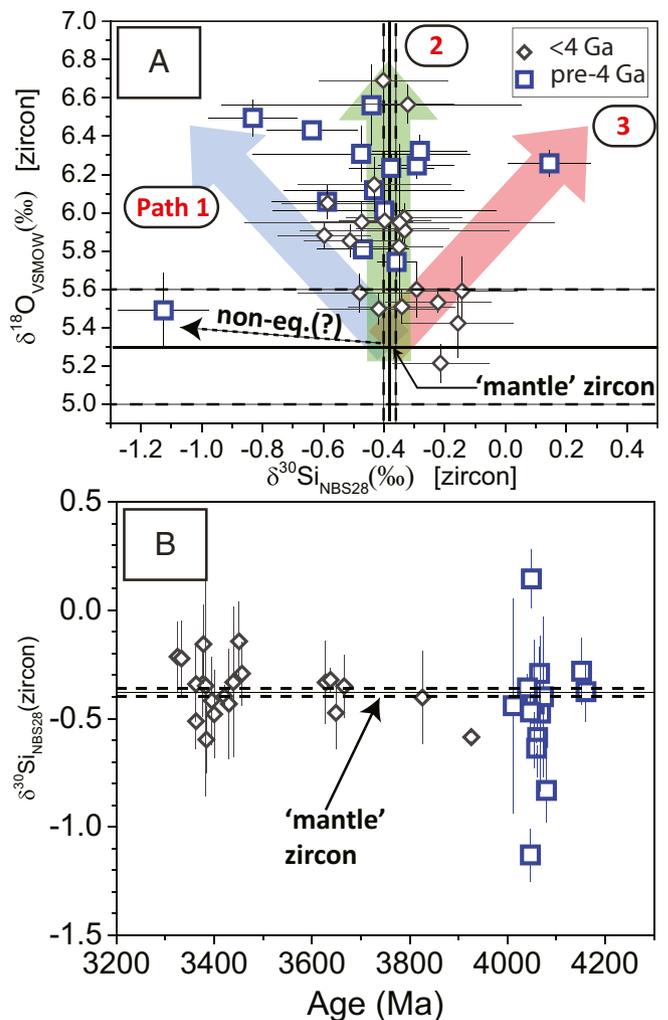
Fig. 5. (*A*) Plot of $\delta^{30}Si$ vs. $\delta^{18}O$ for single Hadean (≥4.0 Ga) and Archean zircon, with schematic weathering paths from Fig. 1, revealing isotopic heterogeneities in both age suites. Mantle-derived zircon yield values of +5.3 ± 0.3 (59) and −0.38 ± 0.02 (Fig. 1) for $\delta^{18}O$ and $\delta^{30}Si$, respectively. (*B*) Zircon $\delta^{30}Si$ plotted against age showing fractionations away from mantle values. Error bars are 1 SE (*SI Appendix*, Table S4) or the SD of multiple ion microprobe analyses on a single grain, whichever is larger. The mantle zircon field is drawn—and reliant upon—high-precision MC-ICP-MS data zircon results (*SI Appendix*, Table S2).

Zircon samples in which both $\delta^{30}Si$ and $\delta^{18}O$ outside the "mantle" zircon field are rare. The most ^{30}Si-enriched detrital zircon is from a 4.05-Ga grain, which is also mildly enriched in ^{18}O relative to the mantle (grain ID = 1–9, $\delta^{30}Si$ = +0.14‰; $\delta^{18}O$ = 6.26‰). As with the positive Si isotope zircons from the LFB granites, this datum implies seawater as the dominant source of $\delta^{30}Si$ (Fig. 1, path 3); note that silicification of volcanogenic sediments from Archean samples display more positive $\delta^{30}Si$ values that range from +0.1–1.1‰, which was also linked to seawater-derived silica (20). The same study showed that Archean felsic schists are fractionated to positive $\delta^{30}Si$ values, which is also qualitatively consistent with the Si- and O isotope data for this zircon.

Conclusions

In many cases, the Si isotopic measurements of crustal zircons with clear input of weathered material into the source magmas, as judged by ^{18}O enrichments, exhibit $\delta^{30}Si$ values indistinguishable from mantle-derived zircon. Thus, correlative analysis of Si- and O isotopes provides a more robust interpretation than either isotopic system alone; in the case of the detrital grains, "path 2" was the most common weathering trajectory. That said, a fraction of the Si measured in Phanerozoic, Archean, and Hadean zircon requires assimilation of silica that interacted with aqueous solutions into the melt protolith(s), ruling out Si derivation exclusively from mantle sources. The range of Si and O isotope compositions recorded in the Hadean zircons is consistent with melt generation from isotopically heterogeneous sources, similar to the migmatite-related formation of Phanerozoic "crustal"-derived I- and S-type granites. This is also contrary to a model in which all Hadean zircon source melts were derived from isotopically homogeneous mafic rocks (38).

The combined $\delta^{18}O$ and $\delta^{30}Si$ measurements restrict the characteristics of Hadean material altered in low-temperature environments. Our preferred model is that some of these involved the anatexis of chemical sediments, possibly felsic schists, and (potentially silicified) metabasalts. This is especially important because the early chemistry of the crust and aqueous solutions are important variables that almost certainly affected early prebiotic or inorganic chemical reactions (39). Archean cherts and highly metamorphosed quartz-pyroxene sediments host some of the earliest proposed evidence for life associated with rocks (40, 41), and an isotopically light carbon inclusion within a Hadean zircon pushes record of a potential biosphere back to 4.1 Ga (12). Our evidence bolsters the case for the existence of a previously undocumented suite of diverse environments—including siliceous sediments—for (pre)biotic chemistry to take hold in the late Hadean.

Materials and Methods

Zircon Samples. Mantle zircons include samples from Orapa (Botswana), and Kimberley Pool, South Africa (42), a megacryst from the Mud Tank carbonatite, and AS-3 zircons. Crustal zircons were extracted from 5 S-type, 4 I-type, and 1 A-type LFB hand samples with ages from 395 to 436 Ma (43–48). Detailed information about sample collection location and zircon geochemistry—including crystallization temperatures—is presented in *SI Appendix* and elsewhere (49, 50). Jack Hills hand samples were collected from the classic locality (5); previously published U–Pb zircon ages are presented elsewhere (50). Fragments from a large crystal from Kuehl Lake were also analyzed, likely from the same locality as 91500 (51, 52).

MC-ICP-MS Solution-Based Measurements. The bulk Si isotope composition was measured using solution MC-ICP-MS techniques, following previously developed methods (53, 54). Sample dissolution was performed using an alkali fusion method. Briefly, between 2 and 10 mg of sample powder was weighed into a silver crucible (99.99% purity), accompanied by ~200 mg of semiconductor-grade NaOH. The crucible was placed into a muffle furnace and heated for 15 min at 720 °C. The resultant fusion cake (inside the crucible) was subsequently immersed in MQ-e water (18.2 MΩ·cm), left to equilibrate overnight, then transferred into precleaned polypropylene

bottles. The solution was diluted further in MQ-e water and acidified to 1% HNO_3 vol/vol.

Silicon was purified for isotope analysis using a single-stage cation-exchange resin ion chromatography procedure. Sample solutions were loaded on to BioRad Poly-Prep columns containing 1.8 mL of precleaned BioRad AG 50W-X12 cation-exchange resin (200–400 mesh). As long as the sample pH is between 2 and 8, silicon will be in solution as a neutral or anionic species and will pass straight through the resin, eluted using MQ-e water—all other major element species will be in cationic form and are quantitatively retained by the resin.

Silicon isotopes were analyzed using a Neptune Plus (Thermo Fisher Scientific) MC-ICP-MS at both the Institute de Physique du Globe de Paris and at the St Andrews Isotope Geochemistry Laboratories, University of St Andrews. The instruments were operated in medium resolution mode (to resolve and avoid polyatomic interferences), and samples were introduced into the instruments using an ESI 75-µL·min⁻¹ PFA microflow nebulizer and an SIS spray chamber. A sample concentration of 2 ppm typically resulted in a signal of between ~14 and 24 V on the ^{28}Si beam (using 10^{11}-Ω resistors), depending on the instrument. Procedural blanks ranged from between 13 and 70 mV on the ^{28}Si beam, which is negligible (<10 ppb Si) relative to the sample. Isotope ratios were measured in static mode, with each measurement consisting of 25 cycles of ~3 s integrations, with a 3-s idle time. Isotope measurements were calculated using the standard-sample bracketing method, with NBS28 (NIST RM 8546) as the bracketing standard, in permil (‰) as follows: $\delta^x Si = [(^x Si/^{28}Si_{sample}/^x Si/^{28}Si_{NBS28}) - 1] \times 1{,}000$; where $x = 30$ or 29, depending on the ratio.

Solution Si isotope data are presented in *SI Appendix*, Table S2. Each datum is calculated as a mean of 3–5 separate measurements, and the uncertainty is calculated as the SD. All paired ^{30}Si and ^{29}Si data plot on a predicted mass-dependent fractionation line (55), indicating that significant interferences on the isotope beams were resolved. Aliquots of the standards BHVO-2 and Diatomite were consistently purified through chemistry and analyzed alongside the sample unknowns. These are also given in *SI Appendix*, Table S2, and are identical to their accepted values (15).

Laser Fluorination O Isotope Measurements. Laser fluorination oxygen isotope analyses were performed at the University of Oregon using a 35-W CO_2 laser in a single analytical session (October 2017). Zircon fragments with weights of ~1.5 mg were reacted with purified BrF_5 reagent to liberate oxygen. The gases generated in the laser chamber were purified through a series of cryogenic traps held at liquid nitrogen temperature and a Hg diffusion pump to remove traces of fluorine gas. Oxygen was converted to CO_2 gas using a small platinum-graphite converter, and then the CO_2 gas was analyzed on an MAT 253 mass spectrometer. Four to seven aliquots of standards were analyzed together with the unknown samples during each analytical session (for detailed analytical methods, see ref. 56). Three UOG (University of Oregon Garnet; $\delta^{18}O$ = +6.52‰) and two Gore Mountain Garnet, UWG2 (University of Wisconsin Garnet-2; $\delta^{18}O$ = +5.80‰) were used in the standard set (57) and varied ±0.07‰.

Ion Microprobe Si- and O Isotope Measurements. Zircons were cast in epoxy along with zircon megacryst chips and AS-3. The South African kimberlite (KIM) reproduced with the lowest SD for Si isotopes by MC-ICP-MS and was thus used as our primary matrix-matched standard for ion microprobe work. Samples were gently polished by hand using disposable 1-µm Al_2O_3 polishing paper, cleaned in successive ultrasonic baths of soapy water and distilled water, dried in a vacuum oven, and then Au coated. A separate mount containing Jack Hills zircons was also prepared. Select crystals were plucked from a preexisting mount (51), recast in epoxy with standards, and polished. All crystals were imaged by cathodoluminescence to help guide ion microprobe spot locations (*SI Appendix*, Fig. S4).

The O- and Si isotopic analyses of zircons were conducted on the University of California, Los Angeles (UCLA) CAMECA *ims*1290 ion microprobe. A 3-nA Cs^+ primary beam, rastering over 10 × 10 µm on the samples, yielded sufficient secondary ion signals ($^{18}O^-$ and $^{30}Si^- \cong 6 \times 10^6$ and 3×10^6 counts per second, respectively) to be collected with Faraday cups (FCs) in dynamic multicollection mode. This configuration allows for simultaneous measurement of $^{16}O^-$ and $^{18}O^-$ on the L'2 and H'2 FCs, respectively, followed by that of $^{28}Si^-$ and $^{30}Si^-$ on C and H1 (all FCs) after one mass jump. The mass resolution (M/ΔM) was set at 2,400 (exit slit #1 on the multicollection trolley) to separate molecular interferences from peaks of interest. One spot analysis is composed of 20 cycles, each of which includes a counting time of 4 s for oxygen isotopes, and of 10 s for Si isotopes. The backgrounds of FCs were determined during the 30-s presputtering before each analysis, and then were corrected for in the data reduction. Secondary electron images were collected after analysis (*SI Appendix*, Fig. S7) to verify analytical spot

locations were free of visible inclusions and cracks. External reproducibilities obtained on the standard KIM zircons were 0.11‰ for $^{18}O/^{16}O$ and 0.23‰ for $^{30}Si/^{28}Si$ (1 SD), which are commensurate with the internal measurement errors, and better than reconnaissance O-isotope results obtained for the Hyperion-II oxygen plasma source (ref. 58 and *SI Appendix*, Fig. S7).

1. Smith JV (1981) The first 800 million years of Earth's history. *Philos Trans R Soc A* 301: 401–422.
2. Sleep NH, Zahnle KJ, Kasting JF, Morowitz HJ (1989) Annihilation of ecosystems by large asteroid impacts on the early Earth. *Nature* 342:139–142.
3. Maher KA, Stevenson DJ (1988) Impact frustration of the origin of life. *Nature* 331: 612–614.
4. Froude DO, et al. (1983) Ion microprobe identification of 4,100-4,200 Myr-old terrestrial zircons. *Nature* 304:616–618.
5. Mojzsis SJ, Harrison TM, Pidgeon RT (2001) Oxygen-isotope evidence from ancient zircons for liquid water at the Earth's surface 4,300 Myr ago. *Nature* 409:178–181.
6. Valley JW, Peck WH, King EM, Wilde SA (2002) A cool early Earth. *Geology* 30: 351–354.
7. Harrison TM (2009) The hadean crust: Evidence from >4 Ga zircons. *Annu Rev Earth Planet Sci* 37:479–505.
8. Cavosie AJ, Valley JW, Wilde SA (2005) Magmatic $\delta^{18}O$ in 4400–3900 Ma detrital zircons: A record of the alteration and recycling of crust in the early archean. *Earth Planet Sci Lett* 235:663–681.
9. Sleep NH, Zahnle K, Neuhoff PS (2001) Initiation of clement surface conditions on the earliest Earth. *Proc Natl Acad Sci USA* 98:3666–3672.
10. Abramov O, Mojzsis SJ (2009) Microbial habitability of the Hadean Earth during the late heavy bombardment. *Nature* 459:419–422.
11. Boehnke P, Harrison TM (2016) Illusory late heavy bombardments. *Proc Natl Acad Sci USA* 113:10802–10806.
12. Bell EA, Boehnke P, Harrison TM, Mao WL (2015) Potentially biogenic carbon preserved in a 4.1 billion-year-old zircon. *Proc Natl Acad Sci USA* 112:14518–14521.
13. Opfergelt S, Delmelle P (2012) Silicon isotopes and continental weathering processes: Assessing controls on Si transfer to the ocean. *C R Geosci* 344:723–738.
14. Opfergelt S, et al. (2012) Silicon isotopes and the tracing of desilication in volcanic soil weathering sequences, Guadeloupe. *Chem Geol* 326–327:113–122.
15. Savage PS, Armytage RMG, Georg RB, Halliday AN (2014) High temperature silicon isotope geochemistry. *Lithos* 190–191:500–519.
16. Savage PS, Georg RB, Williams HM, Halliday AN (2013) The silicon isotope composition of the upper continental crust. *Geochim Cosmochim Acta* 109:384–399.
17. Marin-Carbonne J, Robert F, Chaussidon M (2014) The silicon and oxygen isotope compositions of Precambrian cherts: A record of oceanic paleo-temperatures? *Precambrian Res* 247:223–234.
18. Pollington AD, et al. (2016) Experimental calibration of silicon and oxygen isotope fractionations between quartz and water at 250°C by in situ microanalysis of experimental products and application to zoned low $\delta^{30}Si$ quartz overgrowths. *Chem Geol* 421:127–142.
19. Kleine BI, Stefánsson A, Halldórsson SA, Whitehouse MJ, Jónasson K (2018) Silicon and oxygen isotopes unravel quartz formation processes in the Icelandic crust. *Geochem Perspect Lett* 7:5–11.
20. Abraham K, et al. (2011) Coupled silicon–oxygen isotope fractionation traces Archaean silicification. *Earth Planet Sci Lett* 301:222–230.
21. Savage PS, et al. (2012) The silicon isotope composition of granites. *Geochim Cosmochim Acta* 92:184–202.
22. Poitrasson F, Zambardi T (2015) An Earth–Moon silicon isotope model to track silicic magma origins. *Geochim Cosmochim Acta* 167:301–312.
23. Savage PS, Georg RB, Williams HM, Burton KW, Halliday AN (2011) Silicon isotope fractionation during magmatic differentiation. *Geochim Cosmochim Acta* 75:6124–6139.
24. Qin T, Wu F, Wu Z, Huang F (2016) First-principles calculations of equilibrium fractionation of O and Si isotopes in quartz, albite, anorthite, and zircon. *Contrib Mineral Petrol* 171:91.
25. Bell EA, Harrison TM, McCulloch MT, Young ED (2011) Early Archean crustal evolution of the Jack Hills zircon source terrane inferred from Lu–Hf, 207Pb/206Pb, and δ18O systematics of Jack Hills zircons. *Geochim Cosmochim Acta* 75:4816–4829.
26. Trail D, Bindeman IN, Watson EB, Schmitt AK (2009) Experimental calibration of oxygen isotope fractionation between quartz and zircon. *Geochim Cosmochim Acta* 73: 7110–7126.
27. O'Neil JR, Chappell BW (1977) Oxygen and hydrogen isotope relations in the Berridale batholith. *J Geol Soc London* 33:559–571.
28. Chappell BW, White AJR (1992) I- and S-type granites in the Lachlan Fold belt. *Trans R Soc Edinb Earth Sci* 83:1–26.
29. André L, Cardinal D, Alleman L, Moorbath S (2006) Silicon isotopes in ~3.8 Ga West Greenland rocks as clues to the Eoarchaean supracrustal Si cycle. *Earth Planet Sci Lett* 245:162–173.
30. Robert F, Chaussidon M (2006) A palaeotemperature curve for the Precambrian oceans based on silicon isotopes in cherts. *Nature* 443:969–972.
31. Steinhoefel G, Horn I, von Blanckenburg F (2009) Micro-scale tracing of Fe and Si isotope signatures in banded iron formation using femtosecond laser ablation. *Geochim Cosmochim Acta* 73:5343–5360.
32. Khan RMK, Sharma SD, Patil DJ, Naqvi SM (1996) Trace, rare-earth element, and oxygen isotopic systematics for the genesis of banded iron-formations: Evidence from Kushtagi schist belt, Archaean Dharwar Craton, India. *Geochim Cosmochim Acta* 60: 3285–3294.
33. Zheng YF (1991) Calculation of oxygen isotope fractionation in metal oxides. *Geochim Cosmochim Acta* 55:2299–2307.
34. Wenner DB, Taylor HP, Jr (1973) Oxygen and hydrogen isotope studies of the serpentinization of ultramafic rocks in oceanic environments and continental ophiolite complexes. *Am J Sci* 273:207–239.
35. Muehlenbachs K, Clayton RN (1976) Oxygen Isotope composition of the oceanic crust and its bearing on seawater. *J Geophys Res* 81:4365–4369.
36. Holland HD (1984) *The Chemical Evolution of Atmospheres and Oceans* (Princeton Univ Press, Princeton).
37. Brengman LA (2015) Distinguishing primary versus secondary geochemical and silicon isotope characteristics of Precambrian chert and iron formation. PhD thesis (University of Tennessee, Knoxville), p 238.
38. Kemp AIS, et al. (2010) Hadean crustal evolution revisited: New constraints from Pb–Hf isotope systematics of the Jack Hills zircons. *Earth Planet Sci Lett* 296:45–56.
39. Benner SA, Kim H-J, Carrigan MA (2012) Asphalt, water, and the prebiotic synthesis of ribose, ribonucleosides, and RNA. *Acc Chem Res* 45:2025–2034.
40. Schopf JW, Kudryavtsev AB, Agresti DG, Wdowiak TJ, Czaja AD (2002) Laser–Raman imagery of Earth's earliest fossils. *Nature* 416:73–76.
41. Manning CE, Mojzsis SJ, Harrison TM (2006) Geology, age and origin of supracrustal rocks at Akilia, west Greenland. *Am J Sci* 306:303–366.
42. Haggerty SE, Raber E, Naeser CW (1983) Fission track dating of kimberlitic zircons. *Earth Planet Sci Lett* 63:41–50.
43. Roddick JC, Compston W (1977) Strontium isotopic equilibriation: A solution to a paradox. *Earth Planet Sci Lett* 34:238–246.
44. Ickert RB, Williams IS (2011) U–Pb zircon geochronology of Silurian–Devonian granites in southeastern Australia: Implications for the timing of the Benambran orogeny and the I–S dichotomy. *Aust J Earth Sci* 58:501–516.
45. Williams IS (1992) Some observations on the use of zircon U-Pb geochronology in the study of granitic rocks. *Second Hutton Symposium: The Origin of Granites and Related Rocks* (Royal Society of Edinburgh, Edinburgh) 83:447–458.
46. Chen YD, Williams IS (1990) Zircon inheritance in mafic inclusions from Bega batholith granites, southeastern Australia: An ion microprobe study. *J Geophys Res* 95:17780–17796.
47. Chappell BW, White AJR, Williams IS (1990) Excursion guide B-1. Cooma Granidiorite and Berridale Batholith. *Seventh International Conference on Geochronology, Cosmochronology, and Isotope Geology* (Bureau of Mineral Resources, Geology and Geophysics, Canberra, Australia), pp 1–53.
48. Chappell BW, White AJR (1974) Two contrasting granite types. *Pac Geol* 8:173–174.
49. Trail D, Tailby ND, Sochko M, Ackerson MR (2015) Possible biosphere-lithosphere interactions preserved in igneous zircon and implications for Hadean earth. *Astrobiology* 15:575–586.
50. Trail D, Tailby ND, Wang Y, Harrison TM, Boehnke P (2017) Aluminum in zircon as evidence for peraluminous and metaluminous melts from the Hadean to present. *Geochem Geophys Geosyst* 18:1580–1593.
51. Trail D, et al. (2015) Redox evolution of silicic magmas: Insights from XANES measurements of Ce valence in Bishop Tuff zircons. *Chem Geol* 402:77–88.
52. Trail D, et al. (2007) Constraints on Hadean zircon protoliths from oxygen isotopes, Ti-thermometry, and rare earth elements. *Geochem Geophys Geosyst*, 10.1029/2006GC001449.
53. Georg RB, Reynolds BC, Frank M, Halliday AN (2006) New sample preparation techniques for the determination of Si isotopic compositions using MC-ICPMS. *Chem Geol* 235:95–104.
54. Savage PS, Moynier F (2013) Silicon isotopic variation in enstatite meteorites: Clues to their origin and Earth-forming material. *Earth Planet Sci Lett* 361:487–496.
55. Young ED, Galy A, Nagahara H (2002) Kinetic and equilibrium mass-dependent isotope fractionation laws in nature and their geochemical and cosmochemical significance. *Geochim Cosmochim Acta* 66:1095–1104.
56. Bindeman IN, Bekker A, Zakharov O (2016) Oxygen isotope perspective on crustal evolution on early Earth: A record of Precambrian shales with emphasis on Paleoproterozoic glaciations and Great Oxygenation Event. *Earth Planet Sci Lett* 437: 101–113.
57. Valley JW, Kitchen N, Kohn MJ, Niendorf CR, Spicuzza MJ (1995) UWG-2, a garnet standard for oxygen isotope ratios: Strategies for high precision and accuracy with laser heating. *Geochim Cosmochim Acta* 59:5223–5231.
58. Liu M-C, McKeegan KD, Harrison TM, Jarzebinski G, Vltava L (2018) The Hyperion-II radio-frequency oxygen ion source on the UCLA ims1290 ion microprobe: Beam characterization and applications in geochemistry and cosmochemistry. *Int J Mass Spectrom* 424:1–9.
59. Valley JW, Kinny PD, Schulze DJ, Spicuzza MJ (1998) Zircon megacrysts from kimberlite: Oxygen isotope variability among mantle melts. *Contrib Mineral Petrol* 133: 1–11.